Proceedings of ICFDP 8:
8th International Congress of Fluid Mechanics and Propulsion
Dec 14-17, 2006, Sharm El-Sheikh, Egypt

ICFDP8-EG-167

SIMULATION OF THE DYNAMIC STALL OVER AN OSCILLATING AIRFOIL

Ashraf S. Hussein
Faculty of Computer and Information Sciences, Ain Shams University
Abbassia, 11566, Cairo, Egypt.
ashrafh@acm.org

ABSTRACT

In this paper, a method is presented for the simulation of the boundary layer separation of the flow over a pitching NACA-0012 airfoil in dynamic stall conditions. Computations are performed using a locally developed unsteady two-dimensional Navier-Stokes flow solver. This solver utilizes the finite volume method and employs the upwind flux-difference-splitting (FDS) technique of Roe for the inviscid terms and the viscous terms are centrally differenced. Newton-type sub-iterations are employed to obtain accurate solutions on the moving mesh. The Baldwin-Barth turbulence model is implemented in conjunction with the transition model of Gostelow et al. to simulate realistic flow situations. The transition onset location can either be predicted with Michel's criterion or specified as an input parameter. The accuracy of the developed solver is validated with good agreement against published experimental measurements. Furthermore, the developed flow solver is used to simulate the flow over the NACA 0012 airfoil exhibiting sinusoidal pitching movement in deep-stall conditions and the evolution of the dynamic stall phenomena is satisfactorily captured and investigated.

NOMENCLATURE

a	Speed of sound
c	Airfoil chord
e	Total energy per unit volume
f	Parameter governing the temporal order of accuracy of the scheme
k	Reduced frequency
n	Spot generation rate
p	Static pressure
p_o	Stagnation pressure
$\dot{q}$	Heat flux terms
t	Time
tr	Free stream turbulence
u, v	Cartesian velocities in x,y directions
x, y	Cartesian coordinates
y+	law-of-the-wall variable
C_p	Pressure Coefficient
C_l	Lift Coefficient
C_d	Drag Coefficient
C_m	Moment Coefficient
F, G	Inviscid fluxes
F_v	Viscous flux
J	Transformation Jacobian
M	Mach number
N	Break-down rate parameter
Pr	Prandtl number
Q	Conservation variables
R	Turbulent Reynolds number term in Baldwin-Barth turbulence model; Also, residual term
Re	Reynolds number
S	Semispan
U, V	Contravariant velocities
|V|	Total velocity
$\forall$	Volume
α	Angle of attack
β	Spot spreading half angle
δ	Difference operator
ε	Dissipation term in turbulence model equations
γ	Ratio of specific heats, γ=1.4
λ	Bulk viscosity coefficient
λ_θ	Pressure gradient parameter
μ	Molecular viscosity coefficient
ν	Kinematic viscosity
ρ	Density
σ	Prandtl number
τ	Shear stress tensor
ω	Harmonic oscillation frequency
θ	Boundary-layer momentum thickness
χ	Intermittency function

ς	Spot propagation parameter
∞	Denotes free-stream conditions
ξ,η	General curvilinear coordinates
$\wedge$	Denotes quantities in generalized coordinates
$\sim$	Denotes dimensional value
.	Denotes time derivative
Ω	Magnitude of vorticity

INTRODUCTION

The aerodynamics of an airfoil in unsteady motion is crucial to the performance of rotorcraft. The motion of a typical rotorcraft is complex. The main rotor of a conventional helicopter executes a complicated three-dimensional motion involving flapping (pitching), coning, and lagging [19], figure (1). To achieve a better understanding of the fluid motion, it is reasonable to separately study the individual elements of the airfoil motion (for example, pitching) but recognize that the fluid physics is not so readily separable.

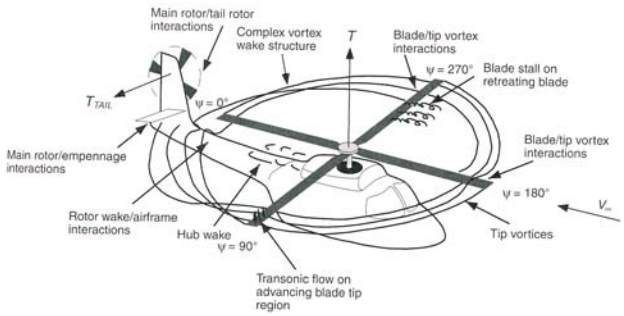

Figure (1) Flow behavior over the rotor of a conventional helicopter, [19].

The understanding of the boundary-layer separation is the key to understand the viscous effects in the unsteady aerodynamics. Qualitatively, boundary-layer separation is the breakdown of the boundary-layer model which divides the flow into two weakly interacting regions (i.e., an irrotational flow occupying most of the fluid volume and a thin viscous region adjacent to the solid boundary). For two-dimensional steady flows, the criterion for boundary-layer separation is well known and indicated by the appearance of zero shear stress at the surface. For two-dimensional unsteady flows, however, the vanishing surface shear stress does not guarantee separation [13]. Rather, the appearance of a zero shear stress and zero velocity point within the fluid in a frame of reference traveling with the separation region seems to be accepted criterion [15] (the "Moore-Rott-Sears" condition).

Boundary-layer separation is an integral part of the dynamic stall process. Three types of stall: light stall, moderate stall, and strong dynamic stall have been observed in literature [6]. The strong dynamic stall phenomenon involves three phases. The lift initially increases as the airfoil pitches up, and continues to increase well past the static stall value, $C_{l,max}$. Towards the end of the upstroke, a vortex begins to form near the leading edge and grows in strength. Towards the beginning of the down-stroke, or shortly thereafter, this vortex is shed from the upper surface, creating a rapid loss in the bound circulation and lift. As this vortex rolls downstream over the upper surface, it causes large reductions in local pressure, and high nose down pitching moments. As the airfoil pitches down, one or more weaker vortices are shed from the upper surface, creating additional fluctuations in lift and pitching moment. The flow eventually reattaches at lower angles of attack.

The pitching moments, along with its large variations are transferred to the vehicle through pitch links, or a flex-beam. These components may fail as a result of the high cycle fatigue that develops. These loads also cause vibrations of the fuselage, passenger discomfort, and structural fatigue. Many electronic components and systems (for example, chips mounted on boards) may experience random failures if the gravity-loads are high enough, and frequent enough to unseat them.

The general focus of the present work is the simulation and visualization of subsonic compressible turbulent flow past an oscillating airfoil in pitching motion at high Reynolds number to provide a virtual "laboratory" whose capabilities are rapidly surpassing what can be observed in any real world. With the right visualization tools, states of behavior can be explored which never be apparent to the naked eye. Extensive surveys for the simulation approaches using Computational Fluid Dynamics (CFD) are given in [4],[18], [17], [1] and [19].

The principle objective of the present paper is to numerically investigate and visualize the phenomena associated with the stages of the unsteady, compressible, subsonic boundary layer separation process for a pitching NACA-0012 airfoil in deep stall conditions using full Navier Stokes flow solver and considering both turbulence and transition from laminar to turbulent. In the present study, the turbulence model of Baldwin and Barth [3] is used to model the turbulent flow regions. The turbulence model is coupled with the transition model of Gostelow et al. [8]. The accuracy of the present solver is validated with satisfactory agreement against published experimental measurements of standard quasi-steady flows (Seifert et al. [16]) and fully unsteady turbulent flows (Anderson et al. [2]) at different Mach number regimes.

The performance of the developed solver is studied for all of the considered test cases and reoptimized to improve the solver efficiency from both storage and computational run time points of view. The solver and its built-in visualization and load prediction capabilities are all developed using C++ language on Windows XP platform.

GOVERNING EQUATIONS

In the present work, the grid remains undistorted and follows the motion of the body at every time instant. The algorithm is based on the compressible, time dependent, Reynolds-averaged Navier-Stokes equations which are written in a curvilinear coordinate system. The equations are solved with finite volume approach and are composed in a conservative form as:

$$\frac{\partial \hat{Q}}{\partial t}+\frac{\partial(\hat{F}-\hat{F}_v)}{\partial \xi}+\frac{\partial(\hat{G}-\hat{G}_v)}{\partial \eta}=0 \quad (1)$$

The subscripts with a comma denote partial differentiation, the subscript v identifies the viscous terms, and the caret (^) over the vectors indicates scaling with respect to the Jacobian J of the coordinate transformation.

where

$$J=\frac{\partial(\xi,\eta,t)}{\partial(x,y,t)} \quad (2)$$

In equation (1), Q is the vector of conserved variables, density, momentum, and total energy per unit volume, such that

$$\hat{Q}=\frac{Q}{J}=\frac{1}{J}\begin{bmatrix}\rho\\ \rho u\\ \rho v\\ e\end{bmatrix} \quad (3)$$

The inviscid flux terms are

$$\hat{F}=\frac{F}{J}=\frac{1}{J}\begin{bmatrix}\rho U\\ \rho U u+\xi_x p\\ \rho U v+\xi_y p\\ (e+p)U-\xi_t p\end{bmatrix} \text{ and} \quad (4)$$

$$\hat{G}=\frac{G}{J}=\frac{1}{J}\begin{bmatrix}\rho V\\ \rho V u+\eta_x p\\ \rho V v+\eta_y p\\ (e+p)V-\eta_t p\end{bmatrix}$$

The contravariant velocities are given by

$$U=\xi_x u+\xi_y v+\xi_t \quad (5)$$

$$V=\eta_x u+\eta_y v+\eta_t$$

The viscous terms are

$$\hat{F}_v=\frac{F_v}{J}=\frac{1}{J}\begin{bmatrix}0\\ \xi_x\tau_{xx}+\xi_y\tau_{xy}\\ \xi_x\tau_{xy}+\xi_y\tau_{yy}\\ \xi_x b_x+\xi_y b_y\end{bmatrix} \text{ and} \quad (6)$$

$$\hat{G}_v=\frac{G_v}{J}=\frac{1}{J}\begin{bmatrix}0\\ \eta_x\tau_{xx}+\eta_y\tau_{xy}\\ \eta_x\tau_{xy}+\eta_y\tau_{yy}\\ \eta_x b_x+\eta_y b_y\end{bmatrix}$$

where

$$b_{x_i}=u_j\tau_{x_i x_j}-\dot{q}_{x_i}$$

$$\dot{q}_{x_i}=-\left[\frac{M_\infty\mu}{Re_{\tilde{L}_R}\,Pr\,(\gamma-1)}\right]\frac{\partial a^2}{\partial x_i} \quad (7)$$

The shear stress and heat flux terms are defined in tensor notations (summation convention implied) as

$$\tau_{x_i x_j}=\frac{M_\infty}{Re_{\tilde{L}_R}}\left[\mu\left(\frac{\partial u_i}{\partial x_j}+\frac{\partial u_j}{\partial x_i}\right)+\lambda\frac{\partial u_k}{\partial x_k}\delta_{ij}\right] \quad (8)$$

The pressure is obtained by the equation of state for a perfect gas

$$p=(\gamma-1)\left[e-\frac{\rho}{2}(u^2+v^2)\right] \quad (9)$$

The above equations have been nondimensionalized in terms of free-stream density, $\tilde{\rho}_\infty$, the free-stream speed of sound, $\tilde{a}_\infty$, and the free-stream molecular viscosity, $\tilde{\mu}_\infty$. Equation (1) is closed by the Stokes hypothesis for the bulk viscosity ($\lambda+2\mu/3=0$) and Sutherland's law for molecular viscosity.

SOLUTION ALGORITHM

The numerical algorithm uses a semi-discrete finite volume formulation, resulting in a consistent approximation to the conservation laws in integral form

$$\frac{\partial}{\partial t}\iiint_{\forall} Q\,d\forall+\iint_S \vec{f}\cdot\vec{n}\,dS=0 \quad (10)$$

where $\vec{f}$ denotes the net flux through a surface S with unit normal $\hat{n}$ containing the (time-invariant) volume $\forall$. Integration of equation (10) over a control volume bounded by lines of constant ξ, and η gives the semi discrete form

$$\left(\frac{\partial \hat{Q}}{\partial t}\right)_{i,j}+\left(\hat{F}-\hat{F}_v\right)_{i+1/2,j}-\left(\hat{F}-\hat{F}_v\right)_{i-1/2,j}+\left(\hat{G}-\hat{G}_v\right)_{i,j+1/2}-\left(\hat{G}-\hat{G}_v\right)_{i,j-1/2}=0 \quad (11)$$

where for convenience,

$$\Delta\xi=\xi_{i+1/2,j}-\xi_{i-1/2,j}=1$$

$$\Delta\eta=\eta_{i,j+1/2}-\eta_{i,j-1/2}=1 \quad (12)$$

The discrete values $\hat{Q}_{i,j}$ are regarded as average values taken over a unit computational cell; similarly, discrete values of $\hat{F}$, and $\hat{G}$ are regarded as face-average values. The convective and pressure terms are differenced using the upwind Flux-Difference-Splitting (FDS) technique of Roe [12] whereas the shear stress and heat transfer terms are centrally differenced. The Monotone Upstream-centered Scheme for Conservation Laws (MUSCL) of Van Leer [13] is used to interpolate state variables at the cell interfaces.

For unsteady airfoil motions, the flow no-slip conditions on the airfoil surface are modified to include the local motion of the surface which also contributes to the pressure on the surface. Therefore the momentum equation normal to the surface (η direction) is solved to predict the pressure for the viscous flow more accurately

$$\partial_\eta p_{wall}=-\frac{1}{\nabla^2\eta}\left[\rho\partial_t\begin{Bmatrix}\dot{x}\\ \dot{y}\end{Bmatrix}_{wall}\cdot\nabla\eta+\partial_\eta p_{wall}\nabla\xi\cdot\nabla\eta\right] \quad (13)$$

where $\dot{x}$ and $\dot{y}$ are the components of the airfoil velocity.

Furthermore, by assuming that the grid is orthogonal at the airfoil surface $\nabla\xi \cdot \nabla\eta = 0$. The far-field boundary condition is imposed implicity by assuming to be essentially inviscid so that the quantities needed for the computation of the flux along the outer boundary are obtained from two locally one-dimensional Riemann invariants [12], [13].

Time Advancement

For nondeforming mesh, equation (1) can be written as

$$\frac{1}{J}\frac{\partial Q}{\partial t} = R(Q) \tag{14}$$

where

$$R = -\left[\frac{\partial\left(\hat{F} - \hat{F}_v\right)}{\partial\xi} + \frac{\partial\left(\hat{G} - \hat{G}_v\right)}{\partial\eta}\right] \tag{15}$$

The time term can be discretized with backward differencing:

$$\frac{(1-\phi)\left(Q^{n+1} - Q^n\right) - \phi\left(Q^n - Q^{n-1}\right)}{J\Delta t} = R(Q^{n+1}) \tag{16}$$

where the superscripts indicate time level. When ϕ=0 the method is first-order temporally accurate; when ϕ=1/2 the method is second-order accurate. This equation is implicit because the right-hand side is a function of the unknown flow variables at time level n+1.

The present solver is advanced in time with implicit approximate-factorization method. The implicit derivatives are written as spatially first order accurate, which results in block-tridiagonal inversions for each sweep. However, the block-tridiagonal inversions are usually further simplified with a diagonal algorithm (with a spectral radius scaling of viscous terms).

Because of the method which the left-hand side is treated for computational efficiency in steady-state simulations (approximate factorization, first-order accuracy), second-order temporal accuracy is forfeited for unsteady computations. One method for recovering the desired accuracy is through the use of sub-iterations. The sub-iteration strategy which is implemented in this solver is termed "physical time sub-iterations (t-TS)," follows Pulliam [14] and Rumsey et al. [15]. Best computational performance appears to occur with 4 to 5 sub-iterations on coarse grids and 2 to 3 sub-iterations on fine grids.

When running steady-state computations, the time step advanced locally in each cell is related to the input Courant number (CFL) number

$$\Delta t \le \frac{CFL}{\left|\nabla\xi\right| t_1 + \left|\nabla\eta\right| t_2} \tag{17}$$

where

$$\begin{aligned} t_1 &= \left|\overline{U}\right| + a + 2\left|\nabla\xi\right|(\mu + \mu_T)\max\left(\frac{4}{3}, \frac{\gamma}{P_r}\right)\frac{M}{Re}\frac{1}{\rho} \\ t_2 &= \left|\overline{V}\right| + a + 2\left|\nabla\eta\right|(\mu + \mu_T)\max\left(\frac{4}{3}, \frac{\gamma}{P_r}\right)\frac{M}{Re}\frac{1}{\rho} \end{aligned} \tag{18}$$

where $\overline{U} = U/\left|\nabla\xi\right|$, and $\overline{V} = V/\left|\nabla\eta\right|$ and U, V, are defined in equation (5).

Turbulence Model

The Baldwin-Barth model [8] solves a single field equation for a turbulent Reynolds number term R

$$\begin{aligned} &\frac{\partial R}{\partial t} + u_j\frac{\partial R}{\partial x_j} = \left(C_{\varepsilon_2} f_2 - C_{\varepsilon_1}\right)\sqrt{RP} \\ &+ \frac{M_\infty}{Re}\left(\nu + \frac{\nu_T}{\sigma_\varepsilon}\right)\frac{\partial^2 R}{\partial x_j^2} - \frac{M_\infty}{Re}\frac{1}{\sigma_\varepsilon}\frac{\partial}{\partial x_j}\left(\nu_T\frac{\partial R}{\partial x_j}\right) \end{aligned} \tag{19}$$

where

$$\frac{1}{\sigma_\varepsilon} = \left(C_{\varepsilon_2} - C_{\varepsilon_1}\right)\frac{\sqrt{C_\mu}}{\kappa^2},\ \nu_T = C_\mu R\, D_1 D_2,$$

$$D_1 = 1 - \exp\left(-\frac{y^+}{A_1^+}\right),\ D_2 = 1 - \exp\left(-\frac{y^+}{A_2^+}\right)$$

and

$$\begin{aligned} f_2 &= \frac{C_{\varepsilon_1}}{C_{\varepsilon_2}} + \left(1 - \frac{C_{\varepsilon_1}}{C_{\varepsilon_2}}\right)\left(\frac{1}{\kappa y^+} + D_1 D_2\right) \\ &\left\{\sqrt{D_1 D_2} + \frac{y^+}{\sqrt{D_1 D_2}}\left[\frac{1}{A_1^+}\exp\left(-\frac{y^+}{A_1^+}\right)D_2 + \right.\right. \\ &\left.\left.\frac{1}{A_2^+}\exp\left(-\frac{y^+}{A_2^+}\right)D_1\right]\right\} \end{aligned}$$

where

$$\mu_T = \rho\nu_T,\ \kappa = 0.41,\ C_{\varepsilon_1} = 1.2,\ C_{\varepsilon_2} = 2.0,$$

$$C_\mu = 0.09,\ A_1^+ = 26,\ \text{and}\ A_2^+ = 26$$

and the production term P is approximated as

$$P \cong \nu_T\Omega^2 \tag{20}$$

At each time step, the equation for the turbulent viscosity is solved separately from the flow equations resulting in a loosely coupled solution process that allows for the easy interchange of new turbulence models. The equation is solved using a backward-Euler time stepping scheme.

Transition Model

The transition model associated with the used turbulence model is the model of Gostelow et al. [8] which permits the calculation of the transition length as a function of the pressure gradient and free-stream turbulence level. The method continuously adjusts the turbulence spot growth in response to changes of the local pressure gradient [16]. The intermittency function in the transitional region is given by

$$\chi(x) = 1 - \exp\left[-n\int_{x_t}^{x_i}\frac{\varsigma}{\tan\alpha}\left(\frac{dx}{U}\right)\int_{x_t}^{x_i}\tan\alpha\, dx\right] \tag{21}$$

where the correlations for the variation of the spot propagation parameter ς and the spot spreading half angle β as function of the pressure gradient parameter λ_θ are

$$\beta = 4 + \frac{22.14}{0.79 + 2.72\exp(47.63\lambda_\theta)} \tag{22}$$

and

$$\varsigma = 0.03 + \frac{0.37}{0.48 + 3.0\exp(52.9\lambda_\theta)} \tag{23}$$

where $\lambda_\theta = (\theta^2/\nu)/(dU/dx)$ with the boundary-layer momentum thickness, θ, and outer-edge velocity, U, The spot generation rate, n, is inferred from the dimensionless breakdown-rate parameter, N, where

$$N = n\varsigma\,\lambda_{\theta t}^3 / \nu, \tag{24}$$

$$N = 0.86\times10^{-3}\exp(2.134\lambda_{\theta t}\ln(tr) - 59.23\lambda_{\theta t} - 0.564\ln(tr)),\ \text{for}\ \lambda_{\theta t} \le 0 \tag{25}$$

and

$$N = N(\lambda_\theta = 0)\times\exp(-10\sqrt{\lambda_{\theta t}}),\ \text{for}\lambda_{\theta t} \succ 0 \tag{26}$$

and where tr denotes the free stream turbulence.

The spot-propagation-rate and the spot spreading half-angle asymptotically approach a maximum value for high negative values of λ_θ, but n is allowed to increase to infinity for high negative values of $\lambda_{\theta t}$, where $\lambda_{\theta t}$ is the pressure gradient at the transition onset location x_t. The value of the intermittency parameter, $\chi(x)$, is zero for $x \le x_t$, and increases downstream from the transition point, asymptotically to a maximum value of unity, which corresponds to fully-turbulent flow. An effective eddy-viscosity for the transitional region is obtained by scaling the turbulent eddy-viscosity computed by $\chi(x)$, i.e. $\mu_{transition} = \chi(x)\,\mu_T$.

RESULTS AND DISCUSSIONS

Before using the developed solver in dynamic stall simulation, this solver is validated against two sets of standard test cases. The first set is the quasi-steady flow computations and the second set is the fully unsteady flow computations. For the quasi-steady flow cases, computations were carried out at the flow conditions of the experimental cases of Seifert et al. (1999) [16]. Their experiments have been performed for the NACA 0012 airfoil at Mach number of 0.65, Reynolds number of 6 millions and angles of incidence between 2 to 11 degrees. For the unsteady flow, computations were carried out at the conditions of the experimental cases of Anderson et al. [2]. Their experiments have been performed for the NACA 0012 airfoil at Mach number of 0.755, Reynolds number of 6 millions and the angle of incidence is oscillated between 0.016 and 2.526 degrees.

Quasi-Steady Flow Validations

The first set of test cases were performed for the flow past a NACA 0012 airfoil at free stream Mach number of 0.65, and Reynolds number of 6 millions and compared to the experimental measurements of Seifert et al. [16] for different values of the angle of attack in the range of between 2 to 11 degrees. The computational grid used for these computations is 193×65 C-type grid [9]. A preliminary grid sensitivity investigation was performed for steady state solutions by varying initial wall spacing, grid density in both directions, and outer boundary location. As a result a grid with minimum normal spacing at the airfoil surface of 2×10-6 chords, with 41 grid points in the wake and with far field boundary extended by 25 chord length from the airfoil surface was chosen. Partial view of the computational grid is shown in figure (2). The computations were performed using different CFL values in the range of 10 to 5 based on the angle of attack because the flow situation was changed from sub-critical to supercritical by increasing the angle of attack. The convergence histories for the computed cases are shown in figure (3) for the computations with Baldwin-Barth turbulence model in conjunction with the transition model of Gostelow et al. The residuals are reduced by around four orders of magnitude in 103 iterations. The CPU time per time step per grid point on a PC computing platform with Pentium IV 1.8 GHz Intel processor with 512 KB cache memory is about 81 μsec.

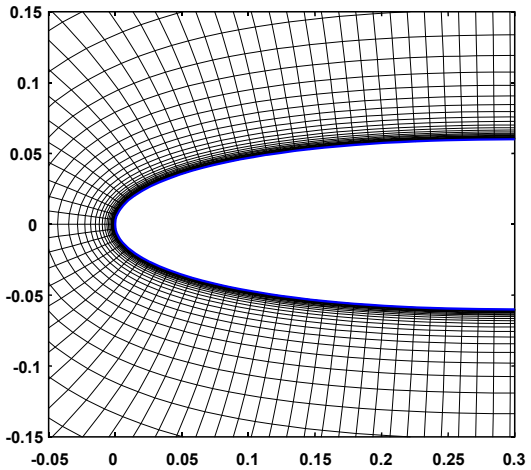

Figure (2) Partial view of NACA 0012 193×65 C-type grid

Figure (4) illustrates the surface pressure coefficient distribution for the computed cases at different angles of attack. As shown the flow situation is changed from sub-critical condition at $\alpha=2^o$ to supercritical at $\alpha=4^o$ and the shock strength was increased by increasing the angle of attack. The shock position at $\alpha=4^o$ is x/c=0.22 chord length from the leading edge and is increased to almost x/c=0.3 chord length by increasing the angle of attack to $\alpha=8^o$ then re-decreased to x/c=0.24 by increasing the angle of attack to $\alpha=11^o$.

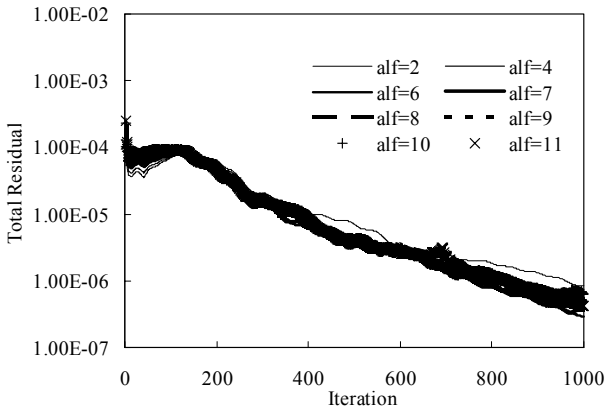

Figure (3) Residual history, Flow past NACA 0012 airfoil, M=0.65 and Re=6×10^6

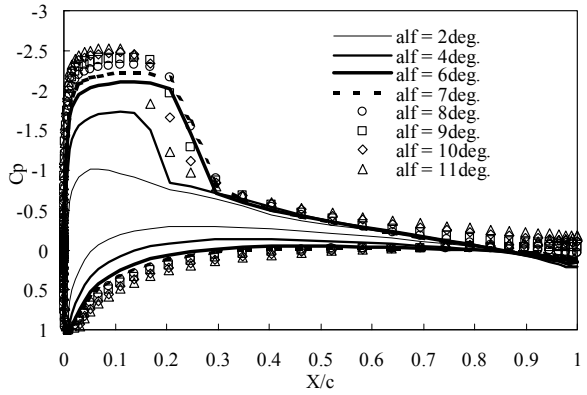

Figure (4) Surface pressure coefficient, NACA 0012 airfoil, M=0.65 and Re=6×10^6

Figures (5) and (6) illustrate the surface pressure coefficient distribution for the computed cases at $\alpha=6^o$ and $\alpha=10^o$ in comparison with the experimental measurements of Seifert et al. [16]. As shown a close agreement with the experimental data is achieved by viscous computation with Baldwin-Barth turbulence model by taking the transition into account. Because no data of the transition onset location where available from the experiment, the transition onset location is computed using Michel's criterion [7]. Michel's criterion predicted the onset location at 44%, 41% chord lengths from the leading edge on the pressure side and at 3%, 1% chord length from the leading edge on the suction side for the two computed cases at $\alpha=6^o$ and 10^o respectively. The corresponding stream lines superimposed on field Mach number contours are illustrated in figures (7) and (8) for the two cases respectively.

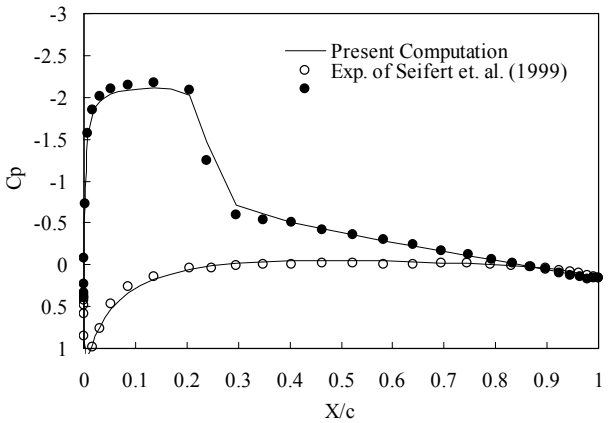

Figure (5) Surface pressure coefficient, NACA 0012 airfoil, M=0.65, Re=6×10^6 and $\alpha=6^o$

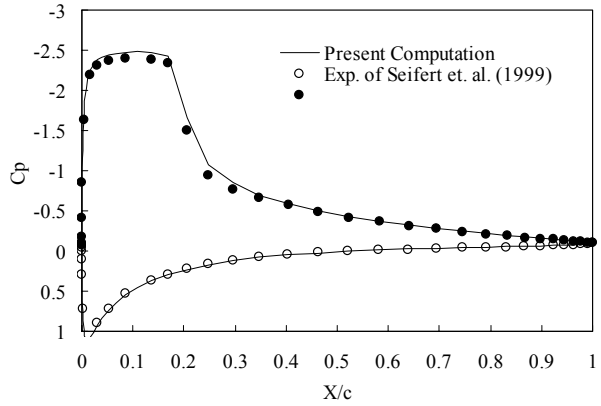

Figure (6) Surface pressure coefficient, NACA 0012 airfoil, M=0.65, Re=6×10^6 and $\alpha=10^o$

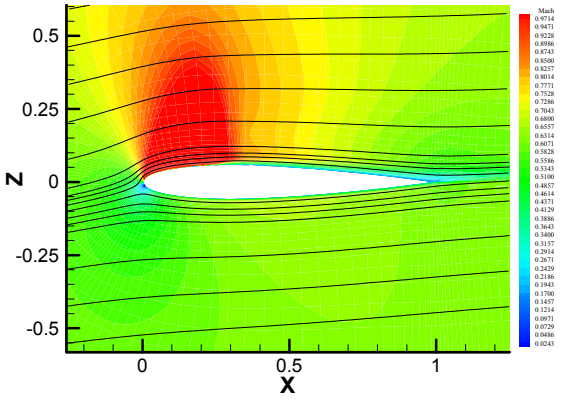

Figure (7) Stream lines and field Mach number contours, NACA 0012 airfoil, M=0.6, Re=6×10^6 and $\alpha=6^o$

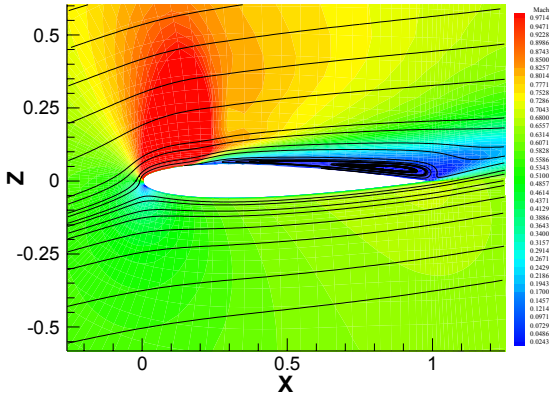

Figure (8) Stream lines and field Mach number contours, NACA 0012 airfoil, M=0.6, Re=6×10^6 and α=10^o

The computed lift and drag coefficient for the computed cases at α=0,2,4,6,7,8,9,10, and 11 degrees are compared to the experimental measurements of Seifert et al. [16] as shown in figures (9) and (10). The maximum difference between the present computation and the experimental data for the drag coefficient is about 28% at α=8^o and the overall average difference is about 9% whereas the maximum difference between the present computation and the experimental data for the lift coefficient is about 3% at α=10^o and the overall average difference is about 1%.

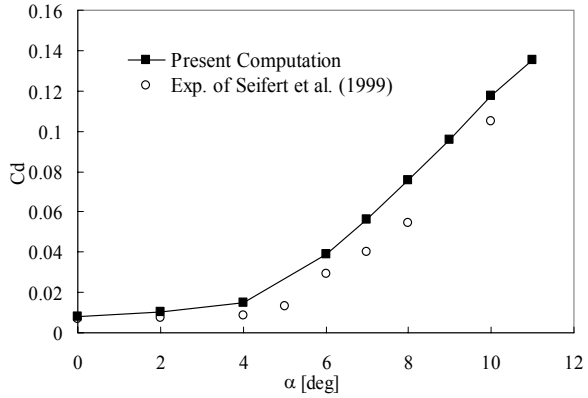

Figure (9) Drag coefficient versus angle of attack, NACA 0012 airfoil, M=0.65 and Re=6×10^6

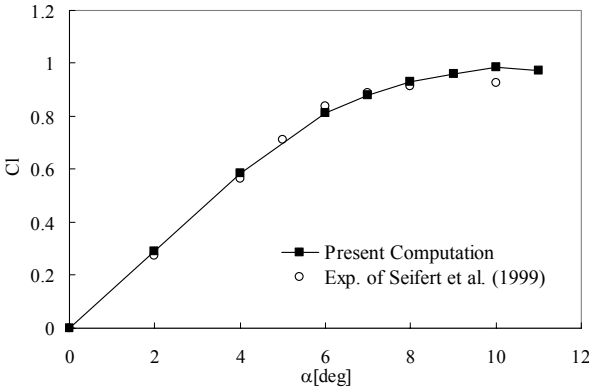

Figure (10) Lift coefficient versus angle of attack, NACA 0012 airfoil, M=0.65 and Re=6×10^6

Unsteady Flow Validations

For all unsteady flow cases presented herein, the airfoil is subjected to a harmonic oscillation which is defined as a function of the angle of incidence variation, α(t),

$$\alpha(t)=\alpha_o(t)+\alpha_1\sin(\omega t) \quad (27)$$

where α_o and α_1 are the mean angle of attack and the amplitude of the harmonic oscillation respectively. In case of oscillating airfoils, the unsteady motion is usually characterized by the similarity parameter, k, known as the reduced frequency of the oscillation. This is defined by

$$k = \omega c/|V_\infty| \quad (28)$$

where ω is the frequency of the oscillation and the airfoil is pitched about the quarter chord axis.

Computational results of both Euler (inviscid flow computations) and Navier-Stokes (viscous flow computations) with Baldwin-Barth turbulence model in conjunction with Gostelow et al. transition model are compared with the published experimental measurements in Anderson et al. [2] for a NACA 0012 airfoil at free stream Mach number of 0.755 and Reynolds number of 6 millions, for viscous computations, undergoing forced pitching oscillation where the mean angle of attack α_o=0.016^o, the amplitude of the pitching oscillation α_1=2.51^o, and the reduced frequency k=0.1628. Results are shown in figures (11-a) to (11-d) which show the computed surface pressure distributions compared to the experimental data at various angles of attack during one pitching cycle. Time accurate computations were performed on the 193×65 C-type grid using a nondimensional time step of 0.1 for Euler computations and 0.03 for Navier-Stokes computations. As shown Navier-Stokes computations give closer agreement with the experimental data than Euler computations. Figures (12) and (13) show a comparison between the computed lift coefficient and pitching moment coefficient and the experimental measurements of [2] for different values of the angle of attack during the pitching cycle. Again, viscous flow computations give closer agreement with experimental measurements.

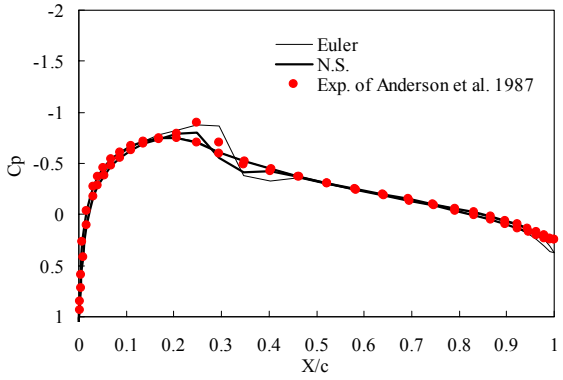

(a) α=1.09°

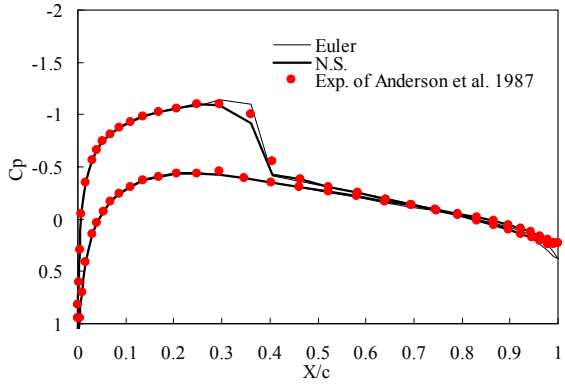

(b) α=2.34°

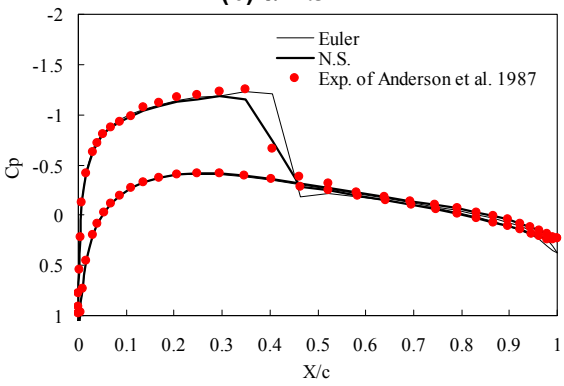

(c) α=2.01°

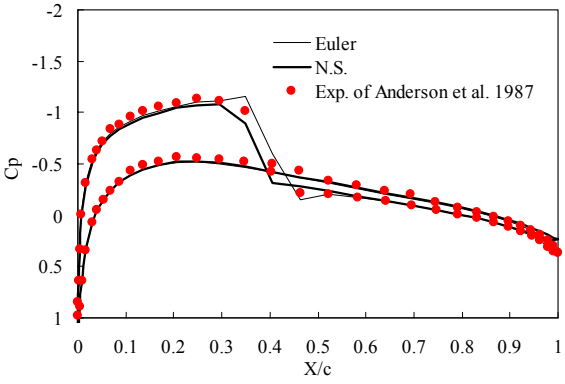

(d) α=0.59°

Figure (11) Surface pressure coefficient, pitching NACA 0012 airfoil, k=0.1628, M=0.755 and Re=6×10^6

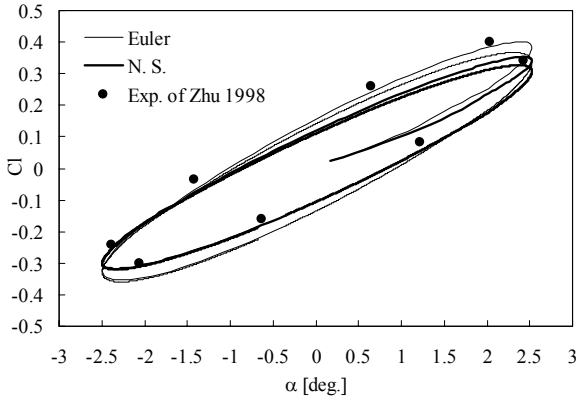

Figure (12) Lift coefficient versus angle of attack, NACA 0012 airfoil, k=0.1628, M=0.755 and Re=6×10^6 (One Pitching Cycle)

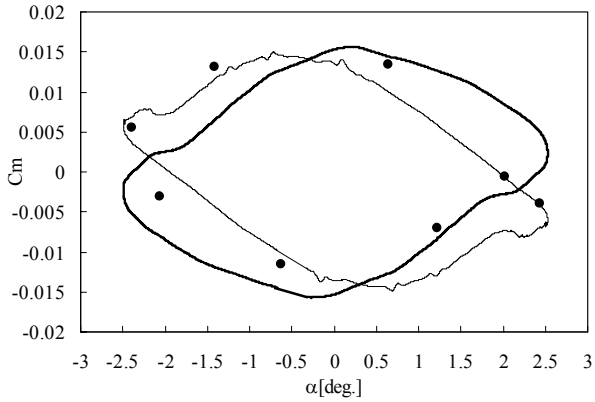

Figure (13) Moment coefficient versus angle of attack, NACA 0012 airfoil, k=0.1628, M=0.755 and Re=6×10^6 (One Pitching Cycle)

Pitching NACA 0012 Airfoil in Deep-Stall conditions

Subsonic compressible flow was simulated around an oscillating NACA 0012 airfoil at deep-stall conditions. Deep-stall flows involve large pitching amplitude and are encountered in helicopter rotors. The free stream conditions are M=0.31 and Re=1,065,000. The mean angle of attack is α_o=10°, the amplitude of the pitching oscillation is α_1=10°, and the reduced frequency is k=0.1. Time accurate computations were performed on the 193×65 C-type grid using a nondimensional time step of 0.005. Initially, quasi-steady computations were performed at the mean angle of attack and considered as the initial solution for the pitching simulation.

Figures (14) to (19) summarize the structures occurring during the dynamic stall via streamlines and surface pressure coefficient distributions. Figures (14) and (15) below show that separation starts at the trailing edge as a clockwise rotating vortex. Subsequently, leading edge separation occurs, Figure (16). For rapidly pitching airfoils, separation may start directly from the leading edge. For high Mach numbers, this situation is assisted by the shock formed close to the leading edge of the profile. During the upstroke, up to an angle of attack of 18

degrees or so, the flow field remains attached. Some increased thickening of the boundary layer is evident on the upper surface as the angle of attack increases. Around 19.43 degrees during the upstroke, the airfoil develops a strong leading edge vortex, seen as a "bump" in the surface pressure distribution in figure (16). The streamlines show considerable amount of separation and recirculation on the upper surface. As the upstroke motion continues the (dynamic stall vortex) DSV is formed, which is rotating clockwise and moves towards the trailing edge of the airfoil, figure (16), while a smaller vortex simultaneously forms between the DSV and the airfoil's wall as shown in figure (17). Subsequently, this vortex breaks up into a pair of co-rotating vortices. As the pitching continues a counter-clockwise rotating vortex forms at the trailing edge of the profile due to the roll-up of a fast moving stream of fluid emerging from the suction side of the profile. As the airfoil reaches the maximum incidence angle, the DSV is shed in the wake. There is a considerable loss in lift, as evidenced by the collapse of the suction peak. During the downstroke motion of the airfoil all vortices are shed in the wake and the flow gradually reattaches starting from the leading edge region, figures (18) and (19).

Figures (20) to (22) show the load hysteresis during a pitching cycle loops for NACA 0012 airfoil. As expected, the lift drops abruptly twice during the downstroke. The pitching moment distribution also shows two large negative peaks, attributable to the large levels of suction that develop near the airfoil trailing edge as the vortex moves over the airfoil. These abrupt variations in the lift and pitching moment directly translate into vibratory loads on the fuselage, and contribute to pitch link fatigue.

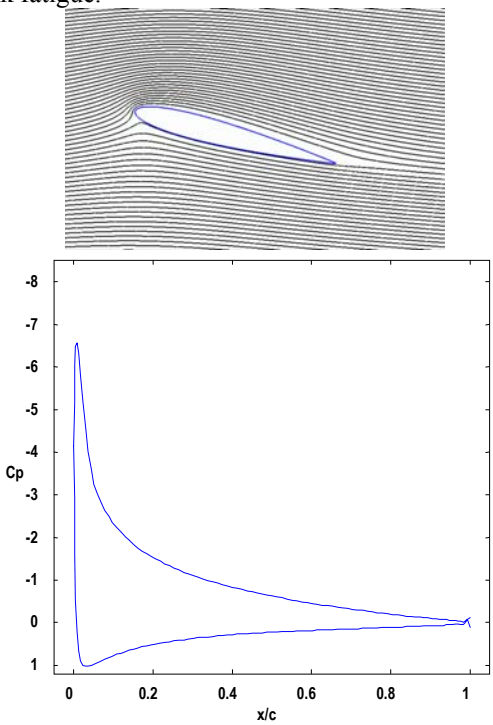

Figure (14) Streamlines and surface pressure coefficient over the NACA0012 airfoil at α=14.62°.

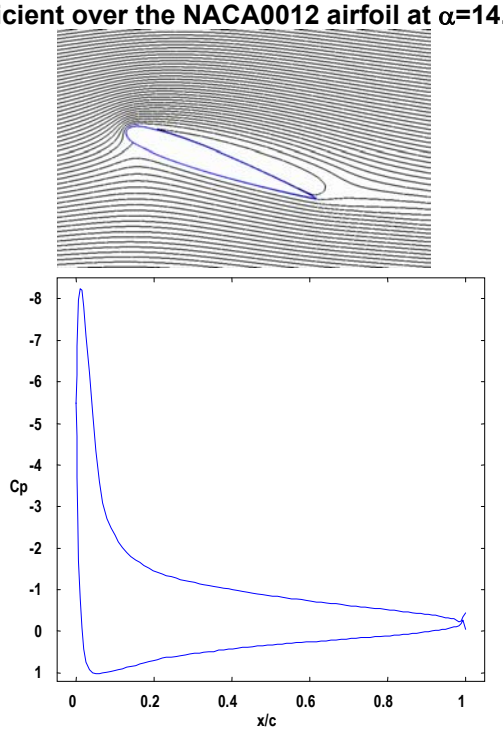

Figure (15) Streamlines and surface pressure coefficient over the NACA0012 airfoil at α=16.51°.

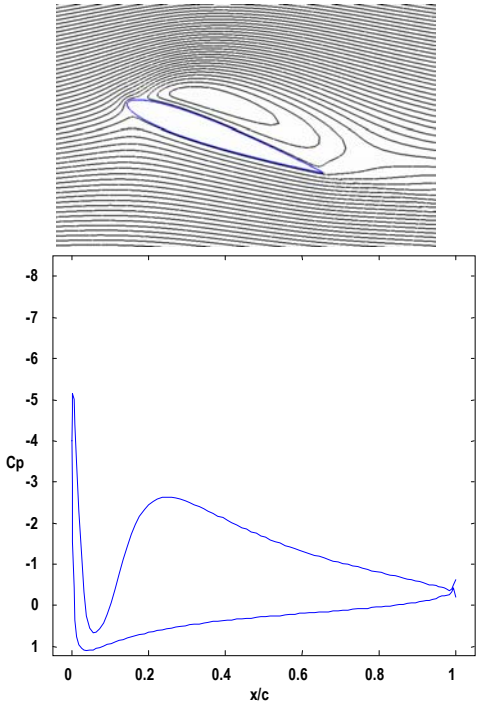

Figure (16) Streamlines and surface pressure coefficient over the NACA0012 airfoil at α=19.43°.

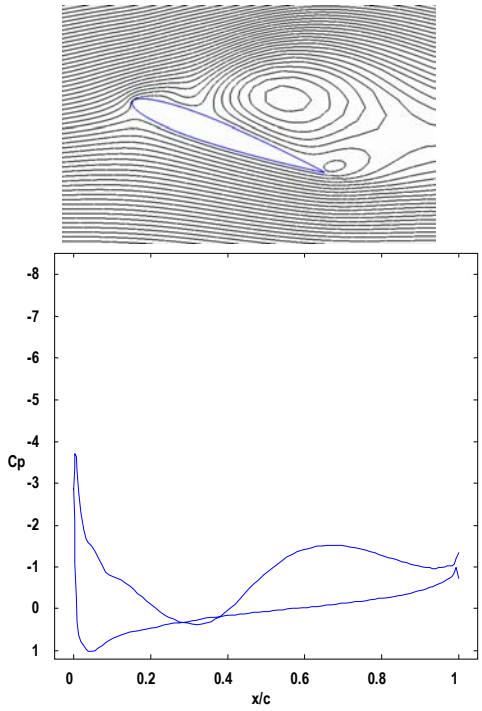

Figure (17) Streamlines and surface pressure coefficient over the NACA0012 airfoil at α=20.0°.

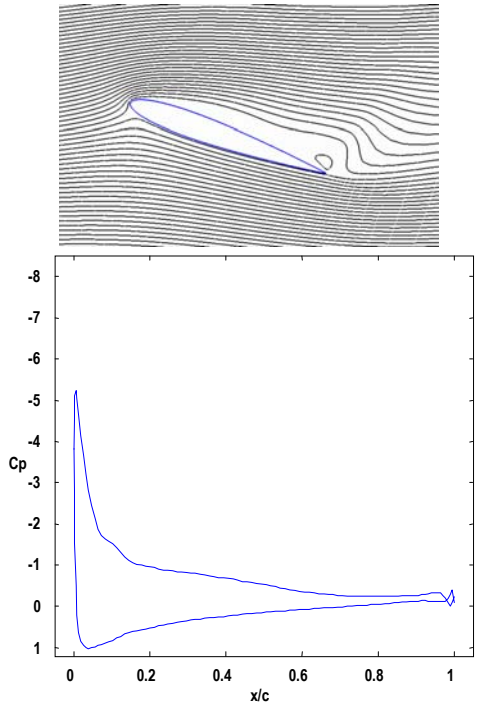

Figure (18) Streamlines and surface pressure coefficient over the NACA0012 airfoil at α=19.66°.

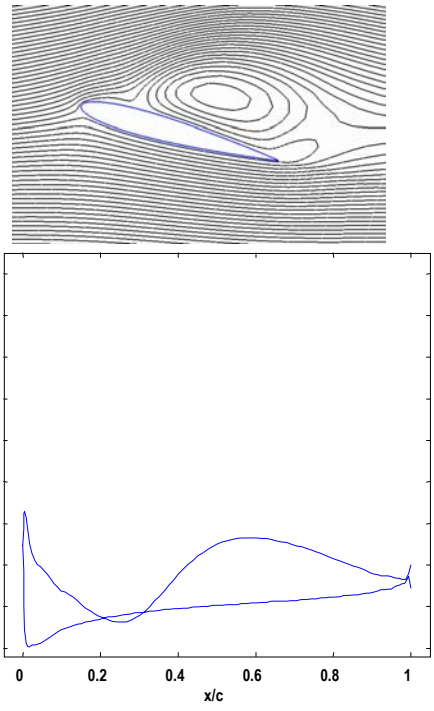

Figure (19) Streamlines and surface pressure coefficient over the NACA0012 airfoil at α=15.31°.

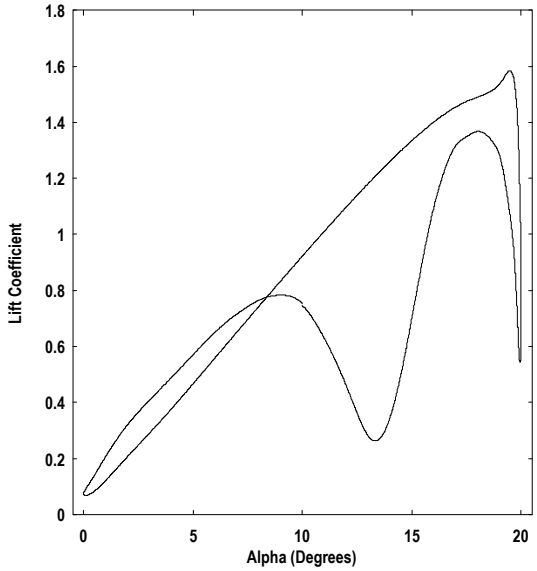

Figure (20) Lift hysteresis loop for the NACA 0012 airfoil

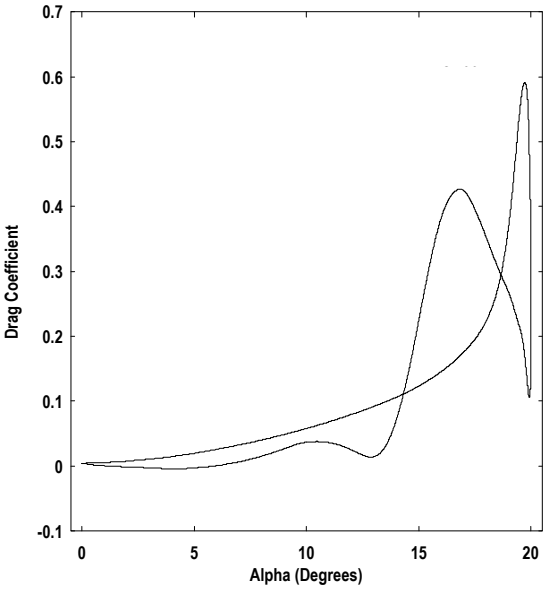

Figure (22) Drag hysteresis loop for the NACA 0012 airfoil.

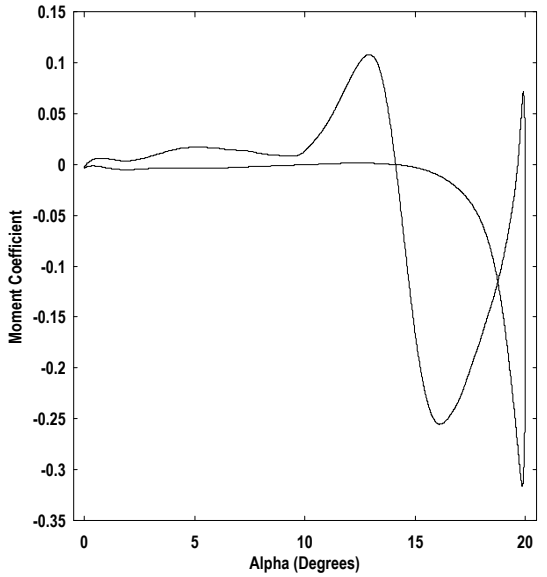

Figure (21) Pitching moment hysteresis loop for the NACA 0012 airfoil

CONCLUSIONS AND FUTURE WORK

A numerical investigation and visualization of the boundary layer separation of flow over a pitching NACA-0012 airfoil has been studied and presented. Computations were performed using a locally developed unsteady flow solver for the unsteady, compressible, Navier-Stokes equations in generalized coordinates with built-in visualization and load prediction capabilities. This solver utilizes the finite volume method and employs the upwind Flux-Difference-Splitting (FDS) technique of Roe for the inviscid terms and the viscous terms are centrally differenced. Newton-type sub-iterations are employed to obtain accurate solutions on a moving mesh. In order to simulate realistic flows, the Baldwin-Barth turbulence model is implemented in conjunction with the transition model of Gostelow et al. Initially, performed computations for quasi-steady and fully unsteady turbulent flows at different flow conditions were compared quantitatively with satisfactory agreement to experimental measurements in order to asses the accuracy of the flow solver. Furthermore, the constructed flow solver has been successfully used to simulate and visualize the flow over the NACA 0012 airfoil exhibiting sinusoidal pitching movement in deep-stall conditions to investigate the process of dynamic stall in subsonic compressible flow. Future work will be in connection with the study of transonic dynamic stall.

REFERENCES

[1] Akbari, M. H., Price, S. J., "Simulation of dynamic stall for a NACA 0012 airfoil using a vortex method," Journal of Fluids and Structures, Volume 17, Issue 6, p. 855-874, 2003.

[2] Anderson, W. K., Thomas, J. L., and Rumsey, C. L., "Extension and Application of Flux Vector Splitting to Unsteady Calculations on Dynamic Meshes," AIAA paper No. 87-1152, 1987.

[3] Baldwin, B. S., and Barth, T. J., "A One-Equation Turbulence Transport Model for High Reynolds Number Wall-Bounded Flows," NASA TM 102847, 1990.

[4] Barakos, G., and Drikakis, D., "An Implicit Unfactored Method for Unsteady Turbulent Compressible Flows with Moving Boundaries," Journal of Computers and Fluids, Vol. 28, No. 3, pp. 899-922, 1999.

[5] Brodeur, R. R., and VanDam, C. P., "Transition Prediction for A Two-Dimensional Navier-Stokes Solver Applied to Wind Turbine Airfoils," AIAA paper 2000-0047, 2000.

[6] Carr, L. W., McAlister, K. W. and McCroskey, W. J., "Analysis of the Development of Dynamic Stall from Oscillating Airfoil Experiments," NASA TN-D-838270, 1977.

[7] Cebeci, T., and Bradshaw, P., "Momentum Transfer in Boundary Layers," Hemisphere Publishing Corporation, 1977.

[8] Gostelow, J. P., Melwani, N., and Walker, G. J., "Effects of Streamwise Pressure Gradient on Turbulent Spot Development," ASME Journal of Turbomachinery, Vol. 118, pp.737-747, 1996.

[9] Hussein A. S., "Simulation of Turbulent Flows Using Full Navier-Stokes Equations on Commodity Computers," Proceedings of the International Conference on Industrial Electronics, Technology and Automation, ERI, IEEE, pp. 34-43, Cairo, Egypt, December 19-21, 2001.

[10] Pulliam, T., "Time Accuracy and the Use of Implicit Methods," AIAA Paper 93-3360-CP, 1993.

[11] Ramamurti, R. and Sandberg, W. C., "Computational Study of 3-D Flapping Foil Flows," AIAA paper 2001-0605, 2001.

[12] Roe, P., "Approximate Riemann Solvers, Parameter Vectors, and Difference Schemes," Journal of Computational Physics, Vol. 43, No. 2, pp. 357-372, 1981.

[13] Rott, N., "Unsteady Viscous Flow in the Vicinity of a Stagnation Point," Quarterly of Applied Mechanics, Vol. 13, No. 4, pp. 444-451, 1956.
[14] Rumsey, C. L., Sanetrik, M. D., Biedron, R. T., Melson, N. D., and Parlette, E. B., "Efficiency and Accuracy of Time Accurate Turbulent Navier-Stokes Computations," AIAA paper 95-1835, 1995.
[15] Sears, W. R., and Telionis, D. P., "Boundary Layer Separation in Unsteady Flow," SIAM Journal of Applied Mechanics, Vol. 28, No. 1, pp. 215-235, 1975.
[16] Seifert, A. and Pack, L. G., "Oscillatory Excitation of Unsteady Compressible Flows over Airfoils at Flight Reynolds Numbers," AIAA paper 99-0925, 1999.
[17] Shelton, A., Abras, J., Jurenko, R., and Smith, M. J., "Improving the CFD Predictions of Airfoils in Stall," AIAA-2005-1227, presented at the AIAA 43rd Aerospace Sciences Meeting and Exhibit, January, 2005.
[18] Smith, M. J., Wong, T.-C., Potsdam, M., Baeder, J. and Phanse, S., "Evaluation of CFD to Determine Two-Dimensional Airfoil Characteristics for Rotorcraft Applications," Presented at the AHS 60th Forum, Baltimore, MD, 2004.
[19] Spentzos, A., Barakos, G. Badcock, K., Richards, B., Wernert, P. and Schreck, S., "CFD Investigation of 2D and 3D Dynamic Stall,"Presented at the AHS 4th Decennial Specialists' Conference on Aeromechanics, San Francisco, California, January 21-23, 2004.
[20] Stepnieewski, W., and Keys, C., "Rotary-Wing Aerodynamics," Dover, New York, pp. 1-42, 1984.
[21] Van Leer, B., Thomas, J. L., Roe, P. L., and Newsome, R. W., "A Comparison of Numerical Flux Formulas for the Euler and Navier-Stokes Equations," AIAA Paper 87-1104-CP, 1987.